2.3 TEM CHARACTERIZATION OF A SIMULTAENOUSLY NEUTRON-IRRADIATED AND HELIUM-INJECTED PM2000 ODS ALLOY

— H. J. Jung, D. J. Edwards, R. J. Kurtz, (Pacific Northwest National Laboratory); G. R. Odette, and T. Yamamoto (University of California, Santa Barbara)

OBJECTIVE

To investigate the irradiated microstructure of PM2000, a Y-Al-O dispersion-strengthened (ODS) iron-based alloy irradiated to a fast neutron dose of 21.2 dpa with simultaneous helium injection at 500°C in the High Flux Isotope Reactor (HFIR).

SUMMARY

Transmission electron microscopy (TEM) discs of PM2000 were coated on one side with a ~4 μm thick NiAl film and irradiated in HFIR to a neutron displacement damage dose of 21.2 dpa at 500°C. The dpa are primarily produced by fast neutrons, while the *in situ* He injection (ISHI) to 1230 appm derives from the thermal neutron two-step ^{59}Ni(n,α) reaction. A uniform He injection profile extends up to about 8 μm below the NiAl coating, hence the remaining material experiences only dpa damage (21.2 dpa at 500°C). This report summarizes analytical TEM analyses to compare the two different regions, i.e., simultaneous He-injection/displacement damage versus displacement damage only, or high and very low He/dpa ratios, respectively. TEM analyses of the He implanted region reveals a high density of small (<2 nm) He bubbles predominantly associated with dislocation loops in the matrix. Because of a very large grain size, no grain or subgrain boundaries were observed in the samples prepared by focused ion beam (FIB) micromachining. The only voids formed were associated with large ODS particles, all of which were amorphous, irrespective of particle size and level of He. The ODS particles range in size from 15-30 nm, and most particles have a single faceted void attached to it that ranges in size from 5 to 15 nm. On the non-implanted side of the sample, no He bubbles could be detected, and faceted voids were found on ~10% of the ODS particles. The He-implanted side contains both <100>{100} and ½<111>{111} dislocation loops and a low density of line dislocations, whereas the un-implanted side possesses predominantly line dislocations with a lower density of dislocation loops. In both regions, nanoscale fcc precipitates exhibiting a cube-on-cube orientation relationship with the bcc matrix were observed. Chemical analysis using energy dispersive x-ray spectroscopy (EDS) indicates this phase is rich in Al and Ti. It was also noted that substantial Cr segregation occurs around the dislocation loops, concurrent with Fe depletion. The clusters of fcc precipitates that do not appear to be associated with the existing loop or line dislocations. The amorphous Y-Al-O particles contain a high Al concentration (>20 at%) and Cr segregation/Fe-depletion at the periphery.

PROGRESS AND STATUS

Introduction

The first-wall and blanket structural materials of future nuclear reactors demand tolerance to a harsh combination of neutron irradiation that produces displacement damage (dpa) and large inventories of transmutation product He. Fusion structures also experience high and time varying mechanical stresses and potentially corrosive chemical environments [1]. Oxide-dispersed strengthened (ODS) ferritic-based alloys are promising candidates to meet these

severe service challenges owing to excellent high-temperature mechanical properties and remarkable radiation tolerance [2,3].

Due to negligible solubility of He in metals and alloys, it precipitates as gas bubbles in the matrix, at dislocations, and at interfaces such as grain boundaries, martensite lath boundaries, and secondary-phase particle-matrix interfaces [4]. While a high density of small He bubbles may hinder dislocation movement, promoting radiation hardening, the development of significant levels of void swelling is of greater concern. This arises because He bubbles that reach a critical size transform into unstable growing voids, potentially causing significant swelling in an otherwise swelling resistant class of alloys [5]. Furthermore, high concentrations at grain boundaries may degrade creep properties and fracture toughness.

Because the alloy composition is fixed to achieve desired material performance, the formation of He in a fusion environment cannot be prevented, only controlled and managed. Thus to realize the potential of ferritic-based alloys for fusion applications, controlling the distribution of He is of critical importance. The most viable path to achieve this goal involves developing alloy microstructures that can hinder the accumulation of He in large bubbles. Minimizing the migration of He to boundaries while preventing the He from accumulating into damaging bubbles can be accomplished by dispersing the He at the interfaces of a very high density of nano-oxide particles. This approach has led to the development of nanostructured ferritic alloys (NFA) such as 14YWT and MA957. PM2000 is a another ferritic based ODS alloy, possessing a much coarser distribution of Y-Al-O particles, as well as a significantly higher levels of Cr and Al to promote better corrosion resistance.

Due to the absence of a neutron irradiation environment producing conditions relevant to fusion reactors, a novel approach, the *in situ* He injection (ISHI) technique, was used to investigate the effects of simultaneous displacement damage and He accumulation on microstructural evolution of candidate alloys, as described in detail by Yamamoto et al. in [7]. Here we present analytical TEM characterization of PM2000 discs irradiated in the High Flux Isotope Reactor (HFIR) using the ISHI approach to produce the He during neutron irradiation.

Specimen Preparation and TEM Characterization Methods

TEM discs of PM2000, coated on one surface with a 4 μm thick NiAl layer, were irradiated as part of the JP27 irradiation experiment in HFIR to a dose of 21.2 dpa at 500°C, with 1230 appm He being injected over the duration of the irradiation. Cross-sectional TEM foils were prepared to characterize features such as He bubbles/voids, dislocation loops, line dislocations, secondary-phase precipitates, and the ODS particles. The cross-sectional foils were prepared using an FEI Quanta 3D FIB/SEM by milling through the NiAl coating to the underlying steel. The foils were finished with low-energy surface cleaning (2 keV Ga^+ ion) at ±3° tilt angles to remove the damaged layer, then further cleaned to remove any remaining FIB artifacts using a Fischione Model 1040 NanoMill. The parameters for the nanomilling are listed in Table 1.

Table 1. Nanomilling cleaning condition

High tension (eV)	Beam current (nA)	Time (min)	Milling size (μm)	Tilt angle (°)	Temperature (°C)
900	165	20 (each side)	40 × 20	± 10	-165

Sample composition was investigated using a JEOL 7600 FEG-SEM equipped with an Oxford Instruments AZtec EDS system. TEM characterization was performed using a JEOL 2010F microscope, operating at 200 keV, and equipped with an Oxford Instruments Link EDS detector.

Table 2. Composition of PM2000 (ODS alloy)

Alloy	Composition (wt.%) with Fe balance									
	Cr	Ti	$Y(Y_2O_3)$	C	Al	W	Mn	Si	Ni	V
PM2000	19.00	0.5	0.5	-	5.5	-	-	-	-	-
PM2000 (EDS)	18.53	0.47	0.29 as Y	-	6.02			0.96	0.14	0.32

Bright-field TEM/STEM images of dislocation loops were acquired using multiple diffraction vectors at two-beam conditions near [001] and [110] zone axes. An approach based on both crystallographic projection and ***g.b=0*** contrast was adopted for loop analysis [8]. Dark-field TEM images were obtained to investigate a second phase fcc precipitate. Energy-Filtered TEM images for elemental mapping were taken using Gatan EELS spectrometer (776 Enfina 1000). Also, STEM-EDS mapping was conducted to visualize the elemental distribution within the analyzed regions.

The nominal composition of PM2000 is listed in Table 2, along with the overall composition measured using energy dispersive x-ray spectroscopy on the non-coated side of the TEM disc.

Results and Discussion

Initial analyses indicated the entire FIB sample is a single grain. An interaction zone between the NiAl coating and the underlying PM2000 alloy was observed and serves as a reference for evaluation of the depth from the sample surface. Elemental mapping revealed this interaction zone essentially involves the diffusion of Ni, and lower levels of Al, into the PM2000 to a depth of ~500 nm. Redistribution of the Cr and Fe also occur to offset the interdiffusion of Ni and Al. Beyond a micron from the interface, the Ni levels approach levels of 0.2 wt.% or less. All analyses were conducted at regions several microns from the NiAl interface, but still well within the uniformly He-implanted layer.

Fig. 1 presents an elemental map that provides an overview of Cr, Fe, Y, Al, and Ti distributions for both the neutron-only irradiated side (top purple box) and ISHI sides (bottom blue box). The first observation concerns regions of Cr-segregation/Fe-depletion independent of the dislocation structure in the neutron-only irradiated side (top purple box). This Cr-segregation is also present in the He-injected side, but differs significantly in that the segregation is closely associated with edge-on dislocation loops (bottom blue box). The Cr and Fe contents appear to be inversely related throughout the foils. The second observation is that Al and Ti show coupled segregation, nominally independent of the Cr-segregation. The segregation of Al and Ti appears to be related to second phase precipitation, as will be discussed later in this report. The third observation is the Cr-rich shell that forms around the periphery of the yttrium-oxide nanoparticles, accompanied with simultaneous Fe-depletion, an observation reported previously by de Castro et al [9], who conducted thermal annealing of an Fe-12Cr ODS alloy at 750 °C for 4, 24 and 96 hours. The thickness of the Cr shell around the particles in the HFIR-irradiated

TEM discs is 10 to 15 nm thicker than that observed in the case of the unirradiated heat-treated ODS alloy, suggesting this Cr-rich shell is kinetically enhanced at the matrix-particle interface during neutron irradiation. The fourth observation is that a high concentration of Al (around 20 at%) is measured within the oxide nanoparticles, which matches the reports by Capdevila et al [10] and Klimiankou et al. [11], at least with respect to the presence of Al in the particles.

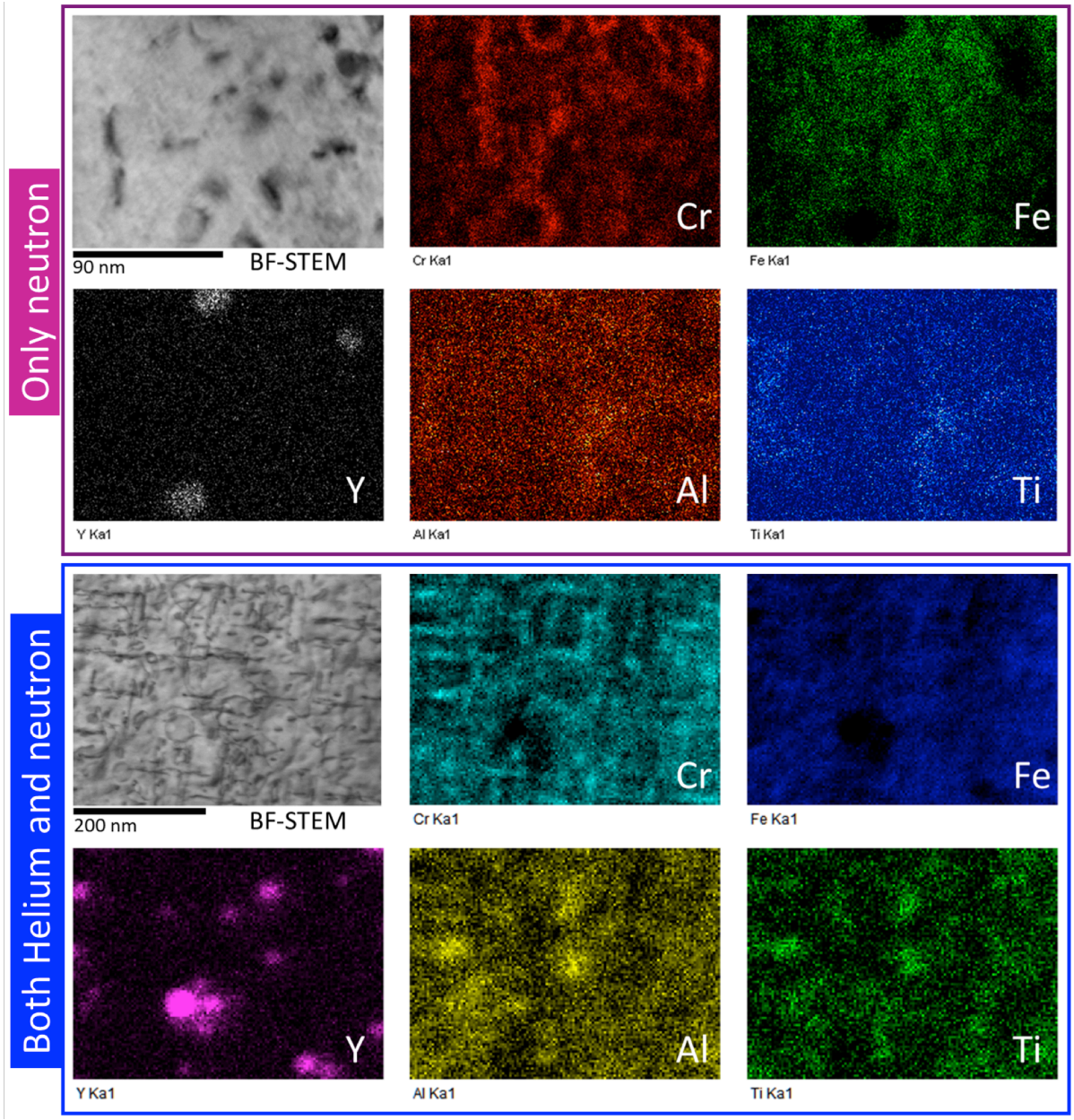

Fig. 1. STEM-EDS elemental mapping of Cr, Fe, Y, Al and Ti from neutron-irradiated side (top purple box) and simultaneously He-injected/neutron-irradiated side (bottom blue box). Bright field-STEM images for STEM-EDS were taken at 15° degree tilting for efficient X-ray signal collection.

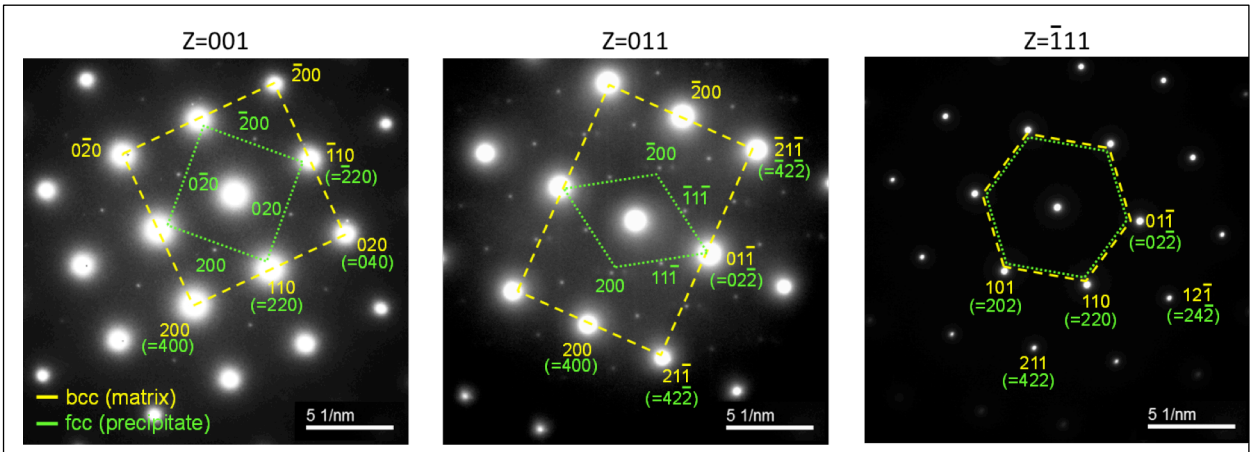

Fig. 2. Selected area diffraction (SAD) patterns of [001], [011], and [111] zones that are representative of the matrix and 2nd phase precipitation common to both sides of the sample. While Fe–based bcc matrix spots are indicated as yellow dot line, 2nd phase fcc precipitate spots are denoted as green dotted line. The 2nd fcc phase has a cube-on-cube orientation relationship to the matrix with a lattice parameter twice that of the bcc matrix.

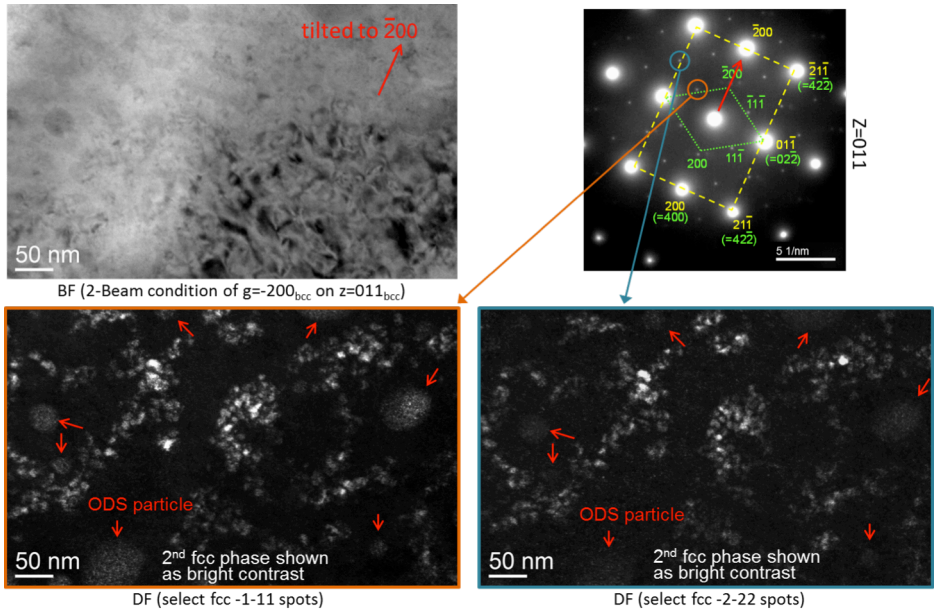

Fig. 3. Bright-field TEM near [011] zone on **g**(200) two-beam condition (top left), SAD pattern of [011] zone (top right), and dark-field TEMs imaged from fcc **g**111 (bottom left) and **g**222 (bottom right) type reflections respectively showing the 2nd fcc phase precipitates and ODS particles.

In order to verify the presence of second phase precipitates suggested from the elemental mapping in Fig. 1, selected area diffraction (SAD) patterns and images were taken at different zone axes such as [001], [110] and [111] as can be seen in Figs. 2 and 3. Note that the diffraction patterns from the two different sides of the sample yielded the same spots, so the He-injection and difference in dislocation structure doesn't appear to impact second phase formation. The diffraction patterns in Fig. 2 reveal less intense, extra reflections that do not correspond to the ferritic bcc lattice; instead, careful examination revealed they belong to an fcc lattice. Alignment of the two crystal structures indicates a cube-on-cube orientation relationship between the precipitates and the matrix. The lattice parameter of the second phase is approximately twice that of the matrix, and may correspond to an ordered DO_3 phase identified by Wittmann et al [12] in an investigation of Fe-Cr-Al alloys. Dark-field TEM (DFTEM) images were taken from corresponding fcc **g**111 and **g**222-type precipitate reflections, revealing precipitate clusters that form independent of the ODS particles and dislocation structures (see Fig. 3). The location of the second phase precipitates corresponds with Al/Ti-enrichment. Capadevila et al [10] also presented evidence of nanoscale regions enriched in Al and Ti, but not Cr, suggesting they were formed during thermomechanical processing alone.

In this irradiated condition, all of the ODS particles on both neutron-only and ISHI regions were found to be completely amorphous based on both the images and the diffraction patterns. High-resolution (HR) TEM from an ODS particle was taken with Fast Fourier Transform (FFT) as seen in Fig. 4. HRTEM shows an amorphous region at the center of an ODS particle with bcc matrix fringes from the overlapping bcc matrix oriented to the [001] zone axis. The FFTs of these images reveal a diffuse amorphous halo from the center of the ODS particle and periodic [001] type arrangement from the bcc matrix. Lattice fringes from the bcc matrix are visible within the ODS particle, but this arises because the amorphous ODS particle is only partially

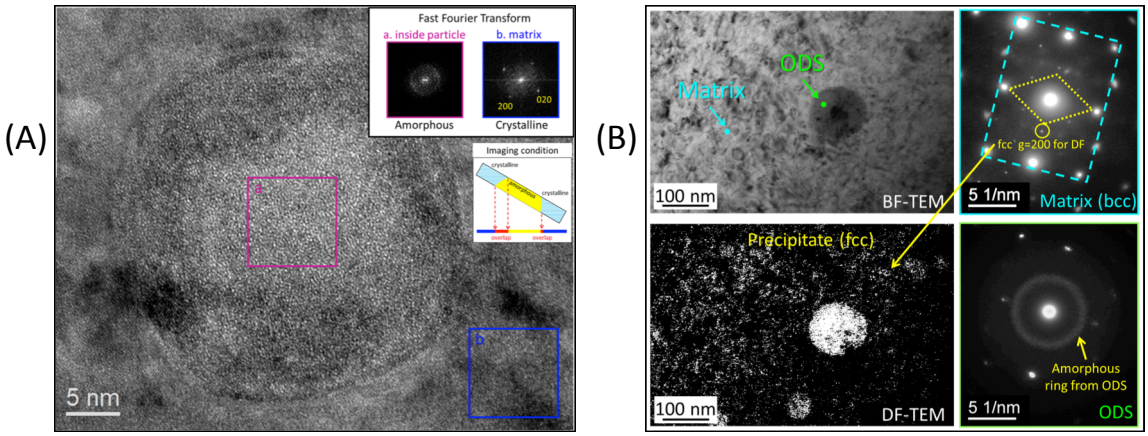

Fig. 4. HRTEM of an ODS particle (A) with FFT inlets from the ODS center (a) and matrix (b) revealing amorphous structure of the particle. A set of TEM and nano-diffraction (B): BFTEM (top left), DFTEM (bottom left) imaged from 200 reflection of 2nd fcc precipitates, and nano-diffraction on matrix (top right) and an ODS particle (bottom right), supporting amorphous property of the ODS particle.

embedded within the foil. The lack of any Moiré fringes in the overlapping regions between the particle and matrix further confirms that the ODS particles are no longer crystalline after irradiation to 21.2 dpa. Further investigation was conducted using a pseudo-parallel electron beam probe of 2~3 nm diameter to acquire nanodiffraction patterns (ND) from the matrix and the ODS particle regions in Fig. 4b. ND on the center of an ODS particle reveals the expected diffuse halo-like ring corresponding to an amorphous structure (bottom left in Fig. 4b) while ND on the matrix shows strong a [110] type-zone bcc pattern and weak [110] type-zone fcc precipitate reflections without the amorphous ring. DFTEM images obtained from an fcc **g**200 spot reveals both the amorphous ODS particles and fcc precipitates because the amorphous halo lies at similar d-spacing with the fcc **g**200 reflection.

Fig. 5 illustrates elemental maps of Cr and Fe taken on the He-injected side of the sample using energy-filtered TEM (EFTEM), which filters only electrons corresponding to a specific atom and images the atomic distribution using the filtered electrons. The EFTEM map can provide a better spatial resolution than that of the STEM EDS maps. The Cr and Fe EFTEMs maps were taken using energy windows of 590±10 eV (Cr $L_{2,3}$ edge) and 720±10 eV (Fe $L_{2,3}$ edge). The Cr is readily segregated around the dislocation loops and Fe is depleted correspondingly in region 1 (red box) of Fig. 5, confirming the trend noticed in the initial elemental mapping presented in Fig 1.

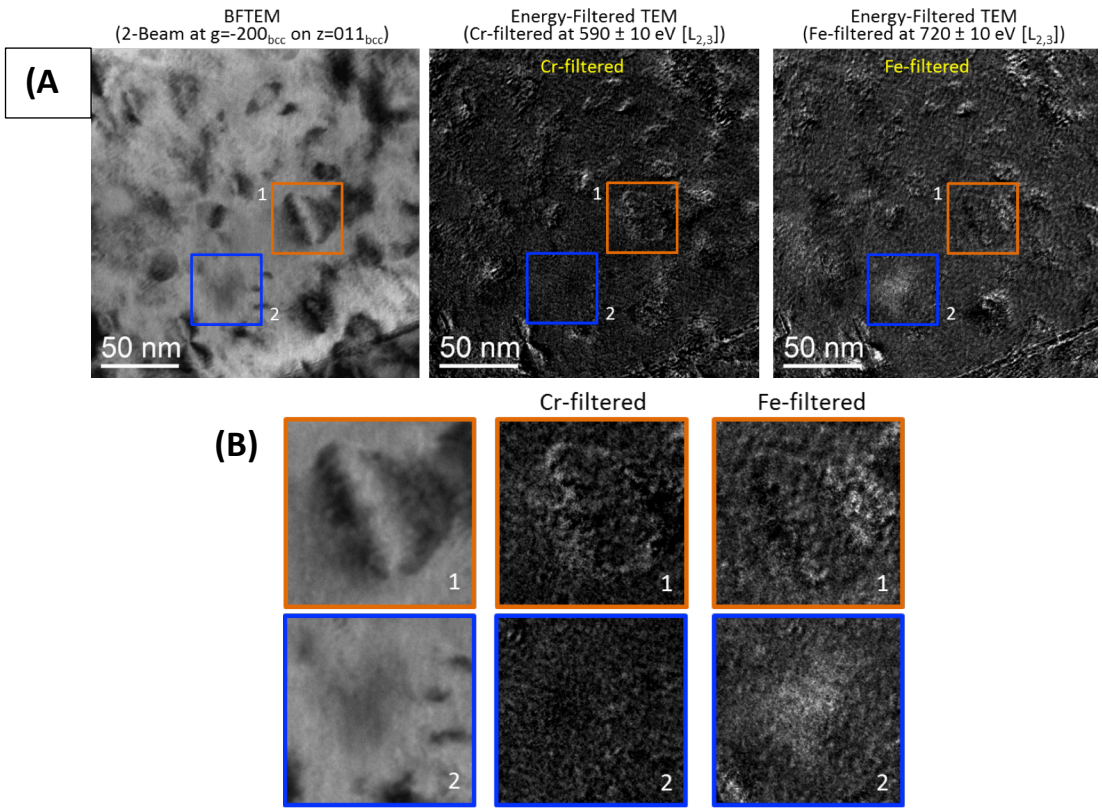

Fig. 5. BFTEM and Cr-filtered and Fe-filtered EFTEMs are presented in (A) and magnified views of region 1 and 2 provided in (B). Region 1 shows the distribution of Cr and Fe on a dislocation loop while region 2 visualizes it on the region without defects.

Having established that significant segregation occurs in irradiated PM2000, we performed initial examinations of the dislocation and He bubble evolution. Figure 6 presents examples of the dislocation structure present in both the He-implanted and He free sides. Both <100> and ½<111> dislocation loops are the dominant dislocation defect observed in the He-implanted side, with a low density of line dislocations present throughout the implanted region. The average size of the <100> loops is approximately 30±9.8 nm, and 18.5±5.3 nm for the ½<111> type loops, with some of the <100> loops extending to over 100 nm in diameter [14]. In the FIB sample taken from the non-implanted side this ratio of loops to line dislocations shifts somewhat in favor of the line dislocations, and the initial impression is that the loops are smaller in diameter compared to those measured in the He-implanted side. The <100>-type loops were found to be consistently enriched with Cr based on the elemental mapping, but this hasn't been confirmed with the ½<111> type loops.

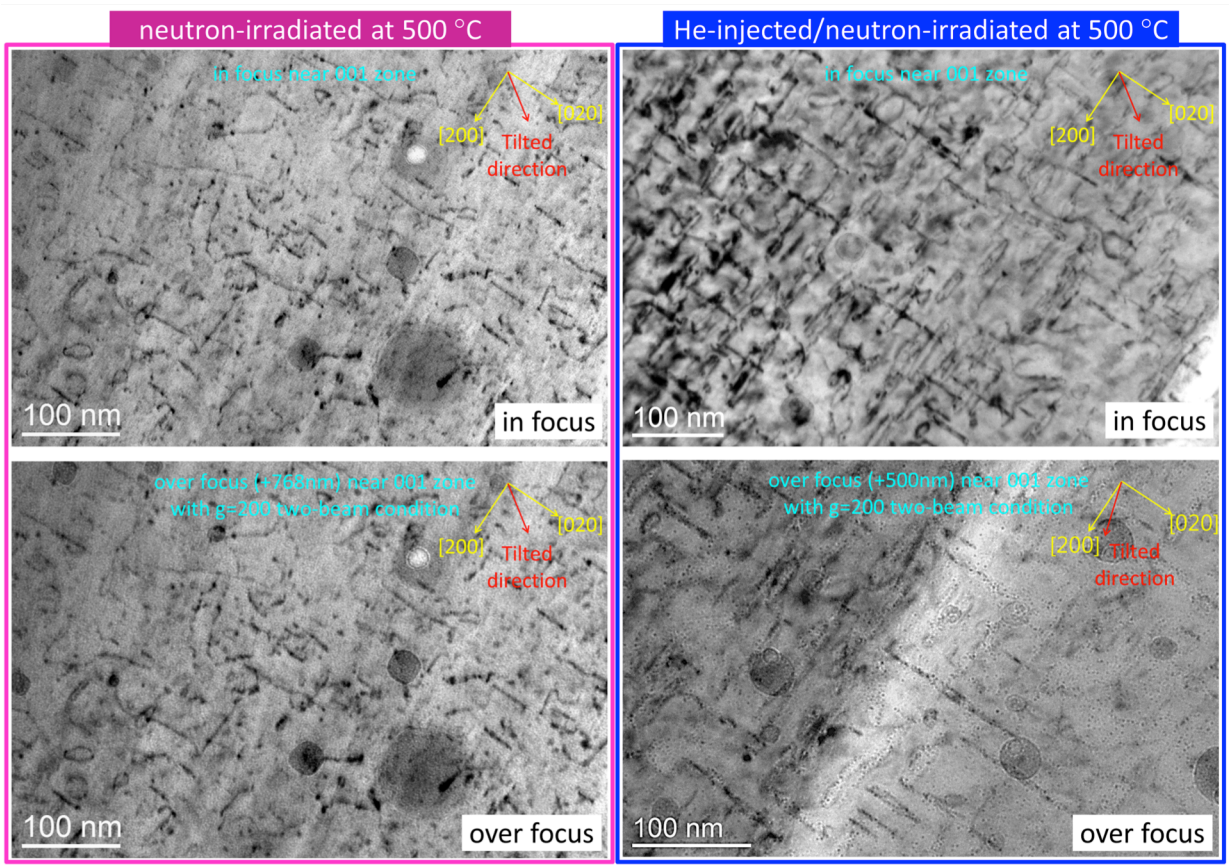

Fig. 6. A set of BFTEM images at in-focus and over-focus near 001 zone on two-beam condition from the non-implanted side (purple box) and the He-implanted side (blue box). The images reveal a mixed dislocation structure of line dislocations and dislocation loops, amorphous ODS particles, and He.

The second observation is that small He bubbles are associated with both the <100> type loops and ½<111> loops, but not necessarily with the line dislocations. The only voids observed in this alloy were formed on the oxide particles, as shown in Figs. 7 and 8. Interestingly, on the non-implanted side less than 10% of the ODS particles possess faceted voids; whereas on the He-injected side of the foil, all of the observed ODS particles were associated with a single faceted void. No He bubbles were observed around the ODS particles.

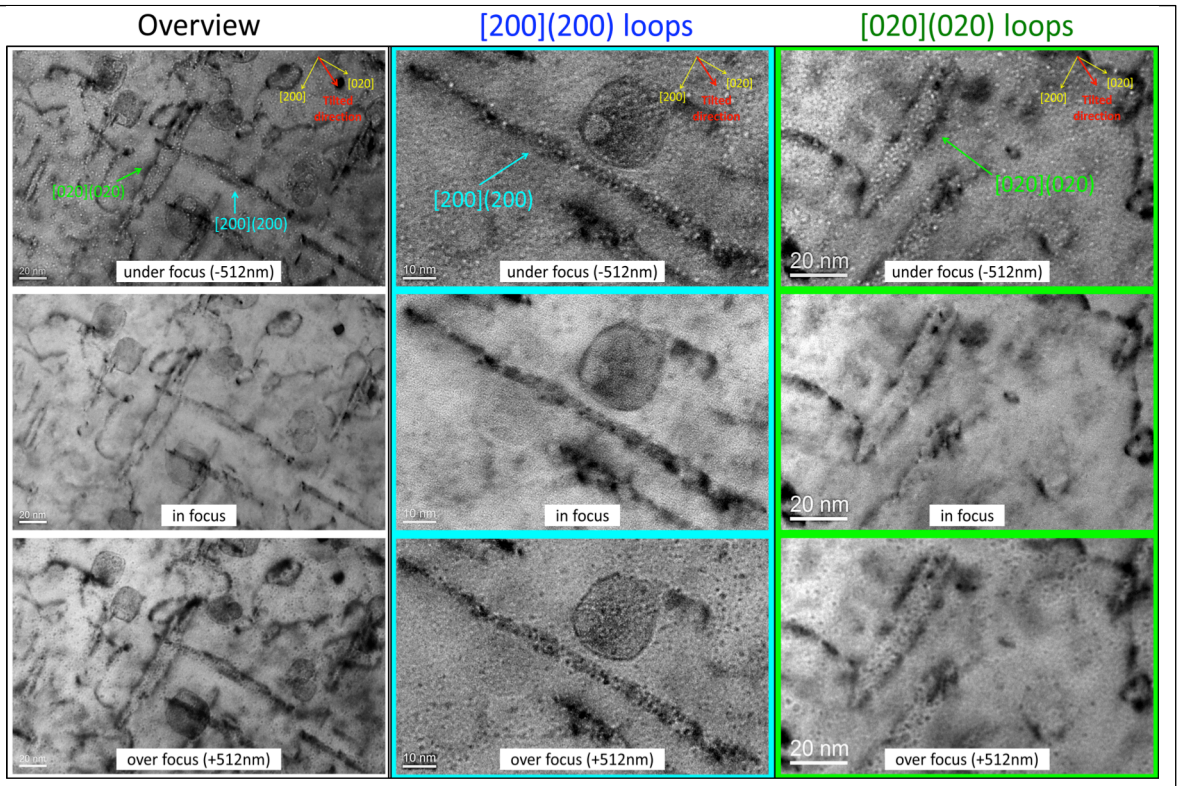

Fig. 7. Three sets of BFTEM images at different magnification with under/in/over-focus near [001] zone from the He-implanted side: sample is tilted off the [001] ZA more toward the [020] direction than [200] to show He bubbles exist inside dislocation loops. Note that contrast of He bubbles are white, none and black respectively at under-focus, in-focus and over-focus.

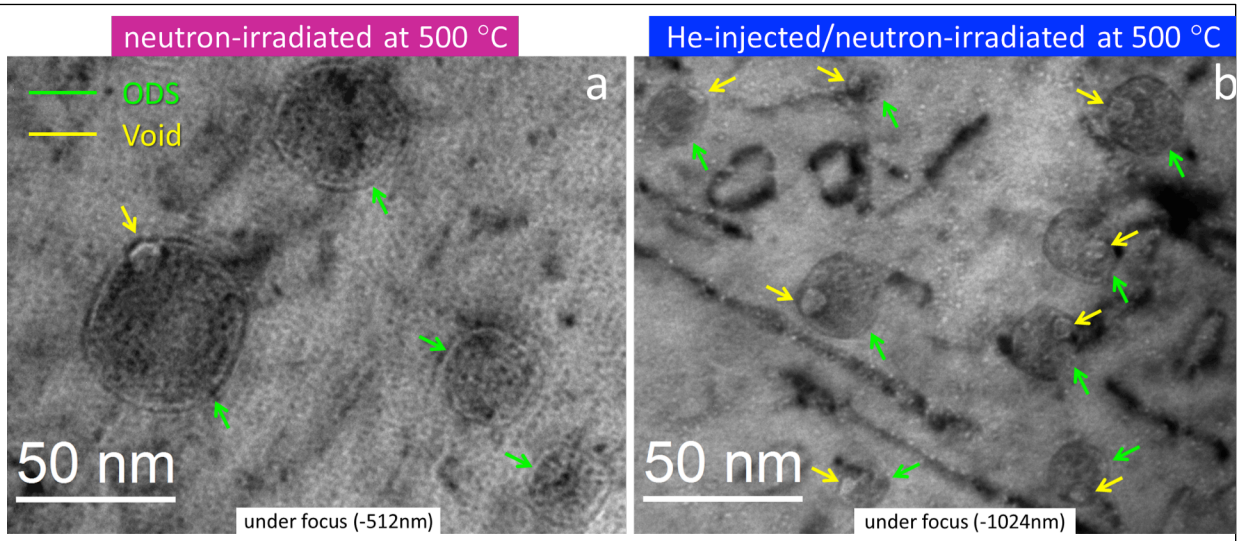

Fig. 8. Under-focused BFTEM images from the (a) non-implanted side versus (b) the He-implanted side showing that virtually all of the ODS particles have faceted voids attached to each particle, whereas only a small fraction of the ODS particles in the non-He implanted side have voids.

A higher magnification view of the loops and bubbles is provided in Figure 7, demonstrating more clearly the association between the two features. In some cases bubbles were visibly arranged in a manner that suggested nucleation and growth around an existing dislocation loop, but the loop itself was invisible because it did not satisfy the **g**·**b** criterion. Our results suggest that He bubbles are forming on the habit plane of the dislocation loops, but in limited cases we find examples of bubbles that appear to follow the periphery of a loop, so further work is needed to understand the relationship between the different loop types and He bubbles. No voids were found other than those associated with amorphous ODS particles, so the presence of large <100> type loops appears to provide sufficient sites to effectively capture the He and nucleate a high density of small bubbles, limiting their ability to reach bubbles of the critical size to form voids.

Future Work

Subsequent analysis is planned to elucidate the nature of the loops and their association with the bubbles. A critical point is to compare the dislocation character between the He-implanted region versus the non-implanted region, and to elucidate the synergism between the He bubbles, dislocation loops, line dislocations and radiation-induced segregation that leads to a relatively stable and low void swelling microstructure.

ACKNOWLEDGEMENTS

This research was supported by the US Department of Energy, Office of Fusion Energy Sciences, under contracts DE-AC06-76RLO1830 and DE-333 FG03-94ER54275. The authors

wish to thank Ruby Ermi and Alan Schemer-Kohrn for their assistance in preparing the samples for TEM analysis.

REFERENCES

[1] N. Baluc, K. Abe, J. L. Boutard, V. M. Chernov, E. Diegele, S. Jitsukawa, A. Kimura, R. L. Klueh, A. Kohyama, R. J. Kurtz, R. Lässer, H. Matsui, A. MÖslang, T. Muroga, G. R. Odette, M. Q. Tran, B. van der Schaaf, Y. Wu, J. Yu, and S.J. Zinkle*, Nucl. Fusion* **47** (2007) S696.
[2] G. R. Odette, M. J. Alinger, and B. D. Wirth, *Annu. Rev. Mater. Res.* **38** (2008) 471.
[3] R. J. Kurtz, A. Alamo, E. Lucon, Q. Huang, S. Jitsukawa, A. Kimura, R. L. Klueh, G. R. Odette, C. Petersen, M. A. Sokolov, P. Spätig, J. W. Rensman, *J. Nucl. Mater.* **386-388** (2009) 411.
[4] H. Ullmaier, *Nucl. Fusion.* **24** (1984) 1039.
[5] R. E. Stoller and G. R. Odette, *J. Nucl. Mater.* **131** (1985) 118.
[6] R. Schäeublin and Y. L. Chiu, *J. Nucl. Mater.* **362** (2007) 152.
[7] T. Yamamoto, G. R. Odette, P. Miao, D. T. Hoelzer, J. Bentley, N. Hashimoto, H. Tanigawa, and R. J. Kurtz, *J. Nucl. Mater.* **367-370** (2007) 399.
[8] B. Yao, D. J. Edwards, and R. J. Kurtz, *J. Nucl. Mater.* **434**, 1-3, (2013) 402.
[9] V. de Castro, E. A. Marquis, S. Lozano-Perez, R. Pareja, and M. L. Jenkins, *Acta Materialia* **59**, 10 (2011), 3927.
[10] J. Ribis and S. Lozano-Perez, *Mater. Lett.* **74** (2012) 143.
[11] C. Capdevila, M. K. Miller, K. F. Russell, J. Chao and J. L. González-Carrasco, *Mater. Sci. Eng. A* **490** 1-2, (2008) 277-288.
[12] M. Klimiankou, R. Lindau, A. Moslang, and J. Schroder, *Powder Metall.* **48** (2005) 277-287.
[13] R. Wittmann, S. Spindler, B. Fischer, H. Wagner, D. Gerthsen, J. Lange, M. Brede, J. Klöwer, P. Schunk, and T. Schimmel, *J. Mater. Sci.* **34** (1999) 1791.
[14] B. Yao, D. J. Edwards, R. J. Kurtz, G. R. Odette and T. Yamamoto, Semiannual Progress Report on Fusion Reactors Materials, DOE/ER-0313/52, June 30, 2012.